

FlexMap: Generalized HD Map Construction from Flexible Camera Configurations

Run Wang¹ Chaoyi Zhou¹ Amir Salarpour¹ Xi Liu¹ Zhi-Qi Cheng²
 Feng Luo¹ Mert D. Pesé¹ Siyu Huang¹

Abstract

High-definition (HD) maps provide essential semantic information of road structures for autonomous driving systems, yet current HD map construction methods require calibrated multi-camera setups and either implicit or explicit 2D-to-BEV transformations, making them fragile when sensors fail or camera configurations vary across vehicle fleets. We introduce FlexMap, unlike prior methods that are fixed to a specific N-camera rig, our approach adapts to variable camera configurations without any architectural changes or per-configuration retraining. Our key innovation eliminates explicit geometric projections by using a geometry-aware foundation model with cross-frame attention to implicitly encode 3D scene understanding in feature space. FlexMap features two core components: a spatial-temporal enhancement module that separates cross-view spatial reasoning from temporal dynamics, and a camera-aware decoder with latent camera tokens, enabling view-adaptive attention without the need for projection matrices. Experiments demonstrate that FlexMap outperforms existing methods across multiple configurations while maintaining robustness to missing views and sensor variations, enabling more practical real-world deployment.

1. Introduction

High-definition (HD) maps provide structured and semantically rich information about road elements (e.g., lane boundaries, dividers, and crosswalks), which is essential for autonomous driving systems such as motion planning (Vazquez et al., 2022; Scheel et al., 2021), map change

¹School of Computing, Clemson University ²School of Engineering & Technology, University of Washington. Correspondence to: Mert D. Pesé <mpese@clemson.edu>.

Preprint. February 2, 2026.

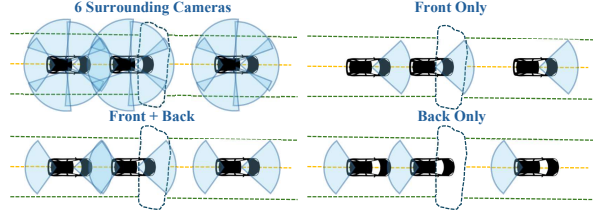


Figure 1. An illustration of HD map construction from flexible camera configurations.

detection, and localization (Jo et al., 2018; Du et al., 2025; Zhang et al., 2025; Wijaya et al., 2024; Ding et al., 2023). Traditional HD map construction relies on dedicated mobile mapping fleets equipped with high-precision sensors and offline SLAM-based processing, resulting in prohibitive costs, which may cost up to \$1,000 per kilometer for creation and updates (Applied Intuition, 2025), and slow update cycles that struggle to keep pace with dynamic urban environments. Recent end-to-end vectorized mapping approaches (Liao et al., 2023; Yuan et al., 2024; Zhou et al., 2024) have demonstrated the feasibility of real-time map generation from onboard sensors, achieving strong performance on standard benchmarks while eliminating the need for offline processing infrastructure.

However, a fundamental challenge remains: enabling HD mapping to be flexible, affordable, and scalable for real-world deployment through data crowdsourced from vehicle fleets. In practice, such fleets are highly heterogeneous, as shown in Figure 1, exhibiting substantial diversity in sensor configurations, from basic monocular cameras to sophisticated multi-camera systems, with wide variation in calibration quality and camera layouts across manufacturers. Moreover, the average vehicle age in both the European Union and the United States now exceeds 12 years (S&P Global Mobility, 2024; ACEA Auto, 2024), meaning most on-road vehicles lack modern sensor suites. This reality makes it essential to design general HD mapping systems that operate effectively under a wide range of camera setups, including those with minimal resources.

To achieve scalable and cost-effective HD mapping, we pro-

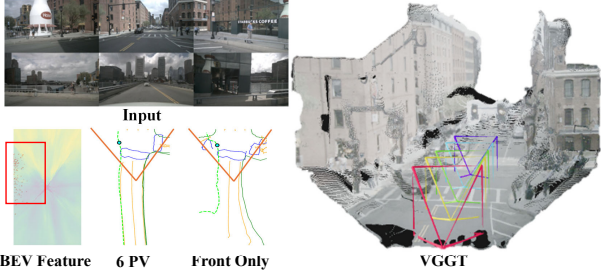


Figure 2. We visualize the BEV feature map used by a BEV-based decoder (e.g., MapTR (Liao et al., 2023)), and a query (green) whose attention for a target location concentrates near a view boundary (red box). While the full six-camera setting (6PV) yields coherent vectors, using only the front camera (1PV) causes fragmentation around the boundary due to missing-view contributions in the BEV features. The VGGT result shows that geometry foundation models can produce geometry-grounded representations even under a sequence of front camera views, motivating a flexible and calibration-free HD map construction pipeline.

pose a new task: HD mapping from uncalibrated cameras, which removes the assumption of precise camera calibration and enables deployment on heterogeneous vehicle fleets. This task is motivated by a critical limitation in current methods: systems must function robustly under flexible camera configurations, yet state-of-the-art approaches exhibit significant architectural constraints in this respect. Approaches such as MapTR (Liao et al., 2023) and GeMap (Zhang et al., 2024) rely on 2D-to-BEV (Bird-Eye-View) (Liu et al., 2023b; Chen et al., 2022) projection modules that require knowledge about precise camera intrinsics and extrinsics for geometric lifting. As demonstrated by recent works (Hao et al., 2025a;b; 2024), these calibration-dependent pipelines suffer severe performance degradation under missing views, miscalibration, or sensor perturbations—conditions that are commonplace in low-cost, crowdsourced deployments.

To further illustrate this limitation, we analyze the cross-attention mechanism in the MapTR (Liao et al., 2023) decoder and observe that query-based attention over BEV features can introduce unintended failure modes. Specifically, when a query lies near the boundary of multiple camera views, the absence of any contributing view can negatively affect the prediction, even if the query point is not strictly within the missing view. As shown in Figure 2, a point associated with a boundary instance lies near the interface between the front and front-left views. When the front-left view is missing, the prediction for this point degrades despite the front view remaining available. This sensitivity highlights the fragility of calibration-dependent, view-coupled attention mechanisms in realistic deployment scenarios. Furthermore, BEV processing as an intermediate step would mean that any error at this step propagates further downstream and compounds, and easily affect quality of the final map construction results.

Therefore, an important question arises: Can we decouple vectorized HD mapping entirely from explicit camera calibration? Recent advances in feed-forward geometry foundation models (Wang et al., 2025) offer a promising alternative. These models can infer dense cross-view geometric relationships and 3D structure from flexible image collections without requiring camera parameters as input. They produce geometry-aware features through learned implicit 3D reasoning. This capability suggests a different design paradigm. Instead of projecting pixels into BEV coordinates using calibrated camera poses, we can produce BEV-consistent map vectors by querying implicit, 3D-aware representations directly. This approach naturally supports various camera configurations, ranging from a single monocular stream to unconstrained multi-camera inputs, while remaining robust to sensor variations.

However, adapting geometry foundation models to vectorized HD mapping introduces two key challenges. First, geometry foundation models are designed to reconstruct static 3D scenes from unordered images. However, driving scenarios involve continuous sequences with dynamic, moving objects that evolve frame by frame. Thus, the model must develop temporal awareness to distinguish persistent road structures from transient entities. Second, since there are no explicit camera poses for 2D-to-BEV projection, the decoder must infer the spatial relationship between image observations and ego-vehicle-centric BEV space. To address these challenges, we introduce **FlexMap**, a feed-forward, camera configuration-free architecture that eliminates explicit 2D-to-BEV projection and instead leverages a pre-trained geometry backbone for cross-view, geometry-grounded features. We designed two key innovations: (1) a spatial-temporal attention module that aggregates the spatial context of the current frame and temporal information to capture the evolution of the dynamic scene and maintain temporal consistency, and (2) an implicit, camera-aware decoder that leverages latent camera tokens to adaptively adjust attention across different cameras, and it enables the model to implicitly infer where to attend. As a result, FlexMap can construct robust HD maps across diverse camera configurations without using explicit camera parameters as input.

Our contributions are summarized as follows:

1. We propose a new task of HD mapping from flexible camera configurations, which removes the dependency on camera calibration and enables scalable deployment on diverse vehicle fleets.
2. We introduce FlexMap, which, to the best of our knowledge, is the first HD map construction framework that accepts variable number of uncalibrated cameras as input and eliminates the need for 2D-to-BEV projection. FlexMap consists of a geometry Transformer backbone,

a novel Spatial-Temporal Enhancement module to aggregate spatial and temporal view information, and a novel camera-aware decoder to enable camera-aware HD map decoding process.

3. Extensive experiments on nuScenes (Caesar et al., 2020) and Argoverse (Chang et al., 2019) show that FlexMap achieves superior performance across diverse camera configurations consistently, especially with missing views and uncalibrated cameras.

2. Related Work

We review prior work on (i) vectorized HD map construction, (ii) robustness under camera corruption and image quality, and (iii) geometry foundation models that provide geometry-aware representations.

2.1. Vectorized HD Map Construction

End-to-end map construction methods predict BEV map semantics directly from on-board sensors, offering a scalable alternative to classical offline map construction pipelines (Shan & Englot, 2018; Shan et al., 2020). Early learning-based approaches often cast mapping as BEV semantic segmentation (Chen et al., 2022; Zhou & Krähenbühl, 2022; Hu et al., 2021; Li et al., 2022b), but rasterized outputs typically require post-processing to obtain structured polylines for downstream planning.

Vectorized approaches instead predict map elements as sets of polylines. HDMapNet (Li et al., 2022a) bridges rasterized BEV predictions to vectors, while VectorMapNet (Liu et al., 2023a) formulates end-to-end vector generation but incurs higher latency due to auto-regressive decoding. The MapTR family (Liao et al., 2023; 2024; Zhou et al., 2024) popularized efficient single-stage, parallel decoding with permutation-equivalent queries, substantially improving both accuracy and practicality. Recent extensions further improve stability and temporal consistency (e.g., streaming/temporal fusion in StreamMapNet (Liao et al., 2024; Yuan et al., 2024)), incorporate geometric priors (e.g., Euclidean relations in GeMap (Zhang et al., 2024)), and address modeling ambiguities via denoising and interaction mechanisms (Hu et al., 2024; Wang et al., 2024a; Kim et al., 2024; Wu et al., 2025). However, these methods generally assume a fixed number of views and rely on camera pose-dependent inputs, limiting their robustness under heterogeneous camera configurations and scenarios with missing views.

2.2. Robust HD Mapping

Robustness under sensor failures has been explored in many applications related to the autonomous driving area (Dong et al., 2023; Zhu et al., 2023; Kong et al., 2024; Ge et al.,

2023). While current vectorized and BEV-based HD map construction methods achieve strong benchmark performance, they typically operate under an idealized sensing setup: a fixed, fully observed, and well-calibrated multi-camera rig, as assumed in nuScenes (Caesar et al., 2020) and Argoverse 2 (Wilson et al., 2023). In practical deployments, however, this premise often breaks; cameras may be temporarily corrupted, physically damaged, absent on certain vehicle trims, or reconfigured over a vehicle’s lifetime, leading to systematic distribution shifts in both view availability and calibration quality. SafeMap (Hao et al., 2025a) explicitly quantifies these failures, showing substantial performance degradation under sensor corruption and missing observations, and thereby underscoring the need for mapping architectures that remain reliable under incomplete and noisy inputs. This vulnerability is not merely a data issue; it is amplified by architectural dependence on explicit geometry modules and calibration-sensitive components, such as pose-conditioned 2D-to-BEV lifting or view transformation pipelines that assume accurate extrinsics/intrinsics (Li et al., 2022b; Liu et al., 2023b; Chen et al., 2022). Consequently, improving robustness to missing views and calibration noise requires designs that reduce sensitivity to rigid camera assumptions while preserving geometric consistency.

2.3. Geometry Foundation Models

To reduce reliance on calibration-sensitive 2D-to-BEV lifting, recent feed-forward geometry foundation models (Wang et al., 2025; 2024b; Keetha et al., 2026) offer a compelling alternative. Models such as VGGT (Wang et al., 2025) learn geometry-grounded representations via objectives including depth prediction, correspondence, and point tracking, enabling cross-view interactions that are anchored in 3D structure without taking camera intrinsics/extrinsics as explicit inputs. These geometry-aware features have already proven effective for downstream tasks such as novel view synthesis (Jiang et al., 2025) and 3D scene reconstruction in driving environments (Zuo et al., 2025; Lin et al., 2025). However, directly leveraging such representations for vectorized HD map construction remains non-trivial, because the target output is not a reconstructed scene but a structured set of BEV polylines with semantic labels. This introduces a notable task and representation gap: the model must translate implicit 3D reasoning into BEV-consistent, topology-aware map elements under diverse and potentially incomplete camera configurations.

3. Methodology

We propose a feed-forward pipeline for high-definition map construction from temporal multi-camera sequences. As illustrated in Figure 3, our method consists of three key components: Feature Extraction (Section 3.2), which lever-

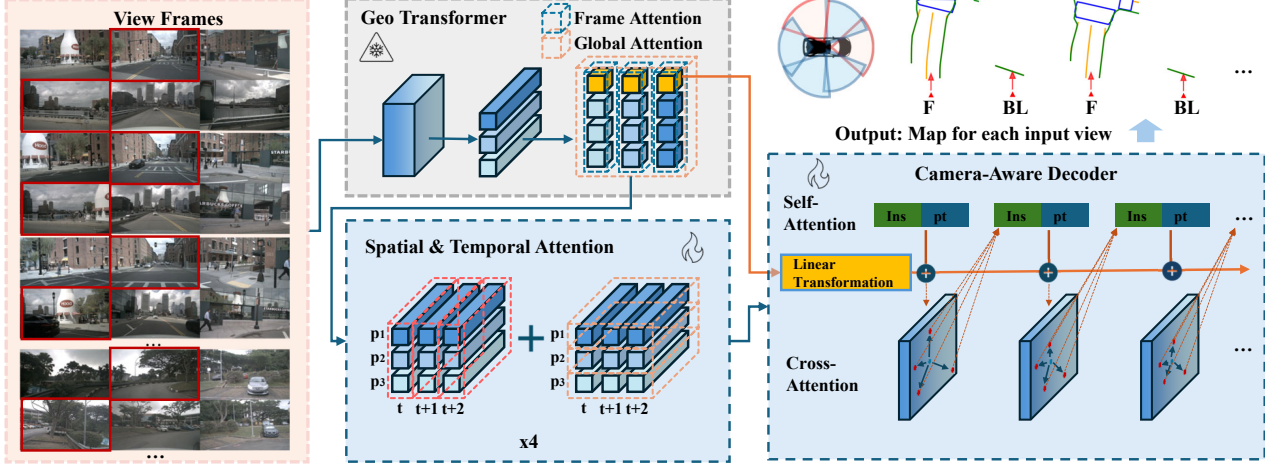


Figure 3. Overview of our method. Multi-camera temporal sequences are processed by a geometry transformer to extract multi-scale features, followed by a spatial-temporal attention module for temporal aggregation. A camera-aware decoder with hierarchical queries then predicts vectorized maps per view. As illustrated, when using the front and back-left cameras as inputs, the model outputs a vectorized map for each provided view.

ages a pre-trained Geometry Transformer and feature fusion; Spatial-Temporal Enhancement (Section 3.3), and a Camera-Aware Decoder (Section 3.4) that predicts vectorized map elements conditioned on camera tokens.

3.1. Problem Setup

Consider S uncalibrated input views $\{\mathbf{I}_s\}_{s=1}^S$, where each image $\mathbf{I}_s \in \mathbb{R}^{H \times W \times 3}$ has height H , width W , and 3 color channels. Unlike conventional methods that assume known camera intrinsics and extrinsics, our framework operates without any calibration parameters. Given these uncalibrated views, our goal is to predict N vectorized map elements $\{(\mathbf{v}_i, c_i)\}_{i=1}^N$, where $\mathbf{v}_i \in \mathbb{R}^{P \times 2}$ represents a polyline as an ordered sequence of P points with (x, y) coordinates, and c_i denotes the class label indicating the type of instance (e.g., divider, pedestrian crossing, or boundary).

3.2. Geometry Transformer

Following VGGT (Wang et al., 2025), we patchify and encode each image into visual tokens using DINOv2 (Oquab et al., 2024). A learnable camera token \mathbf{t}_s is prepended to each view’s tokens. The combined tokens are processed by an alternating-attention transformer: even layers apply frame attention within views for spatial structure, while odd layers apply global attention across views for temporal and cross-view dependencies.

Feature fusion. We extract intermediate features from layers and apply feature fusion. Features are projected to channels, reshaped spatially, and progressively fused through residual convolutions, yielding perspective-view (PV) features $\mathbf{F}_s \in \mathbb{R}^{H' \times W' \times C}$, where C is the feature dimension.

3.3. Spatial-Temporal Enhancement

Multi-camera temporal sequences contain rich but entangled spatial and temporal information. Rather than treating all frames uniformly, we introduce spatial-temporal attention that explicitly separates cross-view spatial reasoning from cross-time temporal reasoning. Given view indices $\{\nu_s\}_{s=1}^S$ (camera identifiers) and time indices $\{\tau_s\}_{s=1}^S$ (timestamp identifiers), we apply two novel attention operations:

Cross-view attention. Frames sharing the same timestamp ($\tau_i = \tau_j$) exchange information across camera views. This captures spatial scene structure. For instance, a lane visible in both front and front-left cameras can be correlated.

Temporal attention. Frames from the same camera ($\nu_i = \nu_j$) exchange information across timestamps. This captures temporal dynamics, lane markings moving through the field of view, or static landmarks providing consistency cues. The design is motivated by the observation that spatial relationships (e.g., overlapping fields of view) are fundamentally different from temporal relationships (e.g., motion continuity). Processing them separately allows each attention module to specialize. The enhanced features $\tilde{\mathbf{F}}_s$ remain in perspective-view space but are enriched with spatial-temporal context from neighboring views and timestamps.

3.4. Camera-Aware Decoder

Different cameras exhibit systematic differences in the geometry and density of observable map elements. As quantified in Figure 4, front and back views contain denser and longer structures with a longitudinal orientation, whereas side views contain fewer, shorter, and lateral segments. Figure 4 further provides a qualitative example of how the

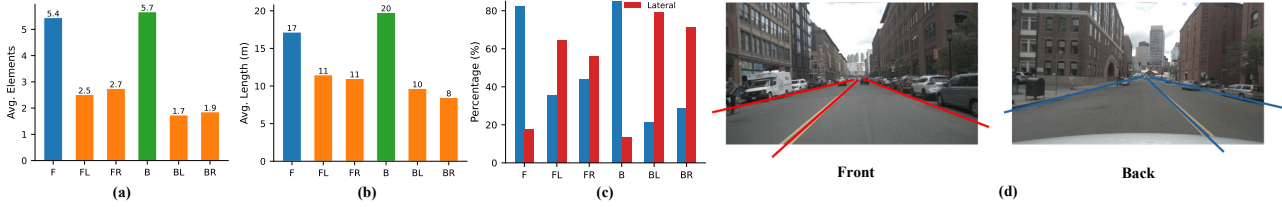


Figure 4. Camera-specific map element statistics for nuScenes (Caesar et al., 2020) dataset after FOV clipping. (a) Average number of elements, (b) average polyline length, (c) orientation distribution (longitudinal vs. lateral). Front and back cameras (F, B) observe denser, longer structures, while side cameras (FL, FR, BL, BR) capture fewer, shorter, and largely lateral elements. (d) shows that vectorized map elements projected in perspective view differ across cameras. The front view primarily contains longitudinal lane structures aligned with the driving direction, whereas the back view exhibits distinct geometry due to the reversed viewing direction.

geometry differs by camera. These camera-dependent statistics motivate a decoder that conditions both query initialization and attention on camera information.

Hierarchical query design. Following MapTR (Liao et al., 2023), we use a hierarchical query structure with N instance embeddings and P point embeddings combined via addition. Each query is defined as \mathbf{q} with a dimension of C .

Camera-conditioned initialization. The camera token \mathbf{t}_s^g encodes view-specific geometry learned during alternating attention. We project it to the query dimension:

$$\mathbf{c}_s = \mathcal{F}_{\text{linear}}(\mathbf{t}_s) \in \mathbb{R}^C. \quad (1)$$

Initial reference points are generated based on both query and projected camera tokens:

$$\mathbf{r}^0 = \sigma(\mathcal{F}_{\text{ref}}([\mathbf{q}; \mathbf{c}_s])) \in [0, 1]^2. \quad (2)$$

This allows initialization strategies to be adaptive, such as initializing anchors along the forward direction for front cameras while using lateral initialization for side cameras.

View-adaptive deformable attention. Each decoder layer applies self-attention followed by deformable cross-attention (Zhu et al., 2021) to perspective-view features, where each query samples K locations. Both sampling offsets and attention logits are camera-aware:

$$\Delta\mathbf{r} = \mathcal{F}_{\text{offset}}([\mathbf{q}; \mathbf{c}_s]), \quad \mathbf{a} = \mathcal{F}_{\text{weight}}([\mathbf{q}; \mathbf{c}_s]). \quad (3)$$

This enables view-specific sampling patterns: front cameras sample along the driving direction to resolve parallel lanes, while side cameras sample laterally to capture boundaries.

Camera-adaptive temperature scaling. Different views benefit from different attention sharpness. Front cameras require sharp attention to disambiguate closely-spaced parallel lanes, while side cameras benefit from smoother attention to aggregate sparse boundary observations. We modulate attention sharpness via a camera-specific temperature τ predicted per attention head:

$$\tau = \sigma(\mathcal{F}_\tau(\mathbf{c}_s)) \cdot (\tau_{\max} - \tau_{\min}) + \tau_{\min}, \quad (4)$$

which scales the attention logits before applying softmax:

$$\hat{\mathbf{a}} = \text{softmax}(\mathbf{a}/\tau). \quad (5)$$

The query embedding $\hat{\mathbf{q}}^l$ is then updated by sampling features at offset locations and aggregating with attention weights:

$$\hat{\mathbf{q}}^l = \sum_{k=1}^K \hat{a}_k \cdot \mathbf{F}_s(\mathbf{r}^l + \Delta\mathbf{r}_k), \quad (6)$$

where $\mathbf{F}_s(\cdot)$ bilinearly interpolates features at the sampled locations. At each layer l , we update the reference points based on the updated query features and camera embedding:

$$\mathbf{r}^{l+1} = \sigma(\mathcal{F}_{\text{ref}}([\hat{\mathbf{q}}^l; \mathbf{c}_s]) + \sigma^{-1}(\mathbf{r}^l)), \quad (7)$$

Query embeddings are finally used to produce a map element prediction via two parallel branches: a classification branch predicting semantic class probabilities over different categories, and a polyline regression branch predicting P normalized 2D coordinates in bird's-eye view.

3.5. Training Objective

Predictions are matched to ground truth via Hungarian matching with permutation-invariant costs (Liao et al., 2023). We apply deep supervision across all L decoder layers and all S input views:

$$\mathcal{L} = \frac{1}{SL} \sum_{s=1}^S \sum_{l=1}^L \left(\lambda_{\text{cls}} \mathcal{L}_{\text{cls}}^{l,s} + \lambda_{\text{pts}} \mathcal{L}_{\text{pts}}^{l,s} + \lambda_{\text{dir}} \mathcal{L}_{\text{dir}}^{l,s} \right) \quad (8)$$

where \mathcal{L}_{cls} is focal loss for classification, \mathcal{L}_{pts} is L1 loss for point coordinates, and \mathcal{L}_{dir} is cosine similarity loss for polyline direction.

4. Experiments

4.1. Experimental Setup

Datasets. We evaluate our approach on the nuScenes dataset (Caesar et al., 2020), which provides 1,000 driving scenes. Each scene contains synchronized multi-camera

Table 1. Comparison with monocular baselines on the nuScenes (Caesar et al., 2020) validation set under different camera input settings. We evaluate our method against baselines that take estimated camera poses as input. For reference, results using ground-truth camera poses are reported in parentheses.

Method	Front only (1PV)				Back only (1PV)				Front+Back (2PV)				All 6 PVs (6PV)			
	AP _{ped}	AP _{div}	AP _{bou}	mAP	AP _{ped}	AP _{div}	AP _{bou}	mAP	AP _{ped}	AP _{div}	AP _{bou}	mAP	AP _{ped}	AP _{div}	AP _{bou}	mAP
MapTR (Liao et al., 2023)	3.7	10.5	10.6	8.3 (40.1)	4.9	12.8	13.9	10.5 (39.9)	4.3	13.9	14.8	11.0 (45.4)	9.0	18.4	17.5	15.0 (53.1)
MapTRv2 (Liao et al., 2024)	4.3	3.9	4.3	4.2 (34.8)	8.0	8.2	10.0	8.7 (38.8)	5.2	7.5	8.4	7.1 (43.8)	13.2	12.0	14.6	13.3 (54.7)
SMN (Yuan et al., 2024)	2.3	10.1	11.1	7.9 (26.7)	4.5	16.7	13.2	11.5 (33.3)	4.5	20.9	17.9	14.4 (41.8)	12.5	20.6	24.6	19.3 (55.0)
GeMap (Zhang et al., 2024)	3.7	7.7	9.9	7.2 (41.2)	8.0	12.2	16.2	12.2 (39.5)	6.7	12.5	15.2	11.4 (48.3)	12.7	14.0	15.7	14.1 (60.9)
MapQR (Liu et al., 2024)	3.4	7.9	8.9	6.8 (32.3)	6.1	12.7	12.8	10.5 (40.7)	5.1	14.1	14.8	11.7 (49.5)	11.6	19.2	20.8	17.2 (62.9)
Ours	42.1	53.6	51.9	49.2	31.4	50.1	52.3	44.6	36.4	52.6	51.7	46.9	40.7	43.0	49.7	44.8

imagery from 6 cameras at 2 Hz, along with high-definition map annotations for three semantic classes: lane dividers, pedestrian crossings, and boundaries. To assess cross-dataset generalization, we additionally evaluate on Argoverse 2 (Wilson et al., 2023). The dataset comprises 1,000 driving logs, each containing 15 seconds of data with RGB images from 7 cameras at 20 Hz, and 3D vectorized map annotations.

To preprocess the nuScenes (Caesar et al., 2020) dataset, we resize images from 1600×900 to 800×450 ($0.5 \times$ scale), then pad to 812×462 to ensure divisibility by the patch size of 14. Ground truth vectors are extracted within a $120m \times 120m$ bird’s-eye view region centered on the ego vehicle. Then we apply camera-specific FOV clipping to only retain vectorized map instances inside the field of view, and finally rotate vectors to camera-centric coordinates. For the Argoverse 2 (Wilson et al., 2023) dataset, cameras have variable resolutions (e.g., front/rear: 2048×1550 , side cameras: 1550×2050). We rescale images by $0.5 \times$ while preserving aspect ratios, then center-pad to exactly 602×602 to ensure divisibility by the patch size of 14.

Evaluation Metrics. We follow standard vectorized map evaluation protocols (Liao et al., 2023; Li et al., 2022a; Liu et al., 2023a), with one key distinction: we evaluate predictions per camera view rather than merging vectors into a unified bird’s-eye-view map. We use Average Precision (AP) to assess detection quality and Chamfer Distance (D_{Chamfer}) to measure geometric alignment between predictions and ground truth. For each map element class, we compute $AP_{\mathcal{T}}$ at multiple Chamfer distance thresholds ($\mathcal{T} \in \{0.5m, 1.0m, 1.5m\}$), then average across all thresholds and classes to obtain the mean AP (mAP). To provide scene-level evaluation, we also rasterize predicted and ground truth vectors onto a 200×400 pixel BEV canvas. Vectors are drawn with 2m line width, producing per-class binary masks. We compute Intersection over Union (IoU) for each class and average to obtain the mean IoU (mIoU). All metrics are averaged across camera views.

Training Details. We train our model with the VGGT (Wang et al., 2025) backbone frozen using AdamW

optimizer with a learning rate 2×10^{-4} and weight decay 0.01. A cosine annealing scheduler reduces the learning rate to a minimum of 1×10^{-5} . Dynamic batch sampling adjusts batch size inversely with sequence length to maintain constant GPU memory usage, processing 48 frames per GPU during training. Sequence lengths are sampled from $S \in \{2, \dots, 24\}$ frames, where S represents the total number of camera views across timestamps. Gradient checkpointing is enabled to reduce memory consumption. The pyramid fusion module extracting features from VGGT layers $\{4, 11, 17, 23\}$, the spatial-temporal enhancer with 4 attention layers and window size 5, and the camera-aware decoder with 6 deformable attention layers are all trained from scratch. Loss weights are set to $\lambda_{\text{cls}} = 3.0$, $\lambda_{\text{pts}} = 4.0$, and $\lambda_{\text{dir}} = 0.05$ for classification, point regression, and direction losses, respectively.

4.2. Baselines

We compare our approach against several state-of-the-art vectorized HD mapping methods. MapTR (Liao et al., 2023) pioneered transformer-based vectorized mapping with permutation-invariant queries and 2D-to-BEV feature fusion (Liu et al., 2023b), establishing a strong baseline. MapTRv2 (Liao et al., 2024) extends MapTR (Liao et al., 2023) with a stronger decoder and temporal modeling. StreamMapNet (SMN) (Yuan et al., 2024) proposes a streaming formulation with temporal fusion in BEV feature space. GeMap (Zhang et al., 2024) introduces geometry-guided constraints based on Euclidean shapes and spatial relations to improve consistency. MapQR (Wang et al., 2024a) further refines vectorized predictions through specialized query designs. For a fair comparison under varying sensor availability, we evaluate all baselines under sensor dropout by masking camera inputs at inference time while keeping their pre-trained weights fixed, and we apply the same field-of-view-based clipping to the output vectorized maps of all methods, including ours.

4.3. Quantitative Results

We evaluate all baselines under two settings: with ground-truth camera poses (values reported in parentheses) and

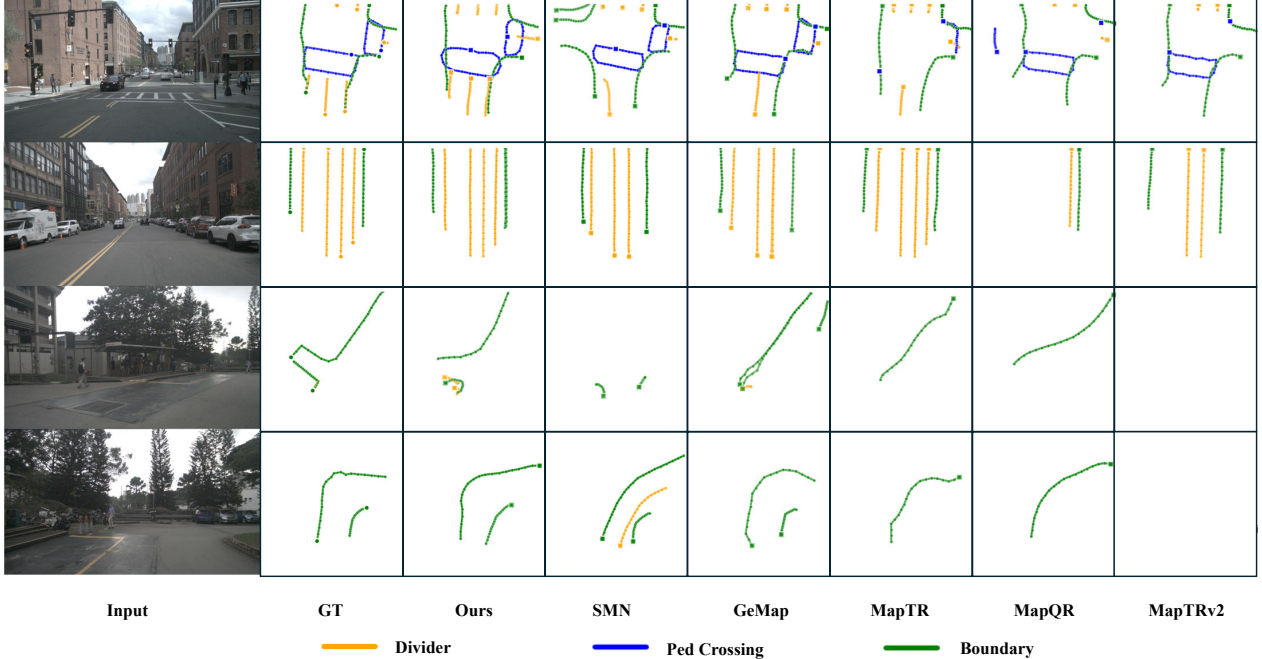


Figure 5. Qualitative comparison on nuScenes dataset. We visualize predictions from different methods across challenging scenarios using a single front camera as input. FlexMap, our pose-free method, produces geometrically consistent predictions (third column) that match ground truth (second column), outperforming the baseline methods with knowledge of ground truth camera pose.

Table 2. Comparison with baselines on the Argoverse 2 (Wilson et al., 2023) validation set under different camera input settings.

Method	Front camera (1PV)				Rear cameras(2PV)			
	AP _{ped}	AP _{div}	AP _{bou}	mAP	AP _{ped}	AP _{div}	AP _{bou}	mAP
MapTRv2 (Liao et al., 2024)	25.0	59.4	47.5	43.9	27.4	60.3	47.6	45.1
MapQR (Liu et al., 2024)	27.8	54.9	46.4	43.0	23.7	61.9	50.7	45.4
Ours	39.9	50.0	51.3	47.0	35.3	55.1	54.6	48.3

pose-free, where camera poses are estimated using a pre-trained VGGT model (Wang et al., 2025) with additional alignment. Since existing baselines require camera poses at inference time, whereas our method operates without any pose input, the pose-free setting provides the most meaningful comparison. Table 1 reports results across different camera configurations. Our pose-free approach achieves 49.2 mAP (1PV front), 44.6 mAP (1PV back), 46.9 mAP (2PV), and 44.8 mAP (6PV), substantially outperforming baselines, which struggle in the absence of accurate poses. Although baselines exhibit strong performance when ground-truth poses are available (e.g., MapQR (Liu et al., 2024) achieves 62.9 mAP in the 6PV setting), our method achieves better performance across 1 and 2 PV settings without requiring any pose information.

In the following experiments, we assume that baselines are provided with accurate camera poses at inference time. We further evaluate our method on the Argoverse 2 dataset (Wilson et al., 2023). As shown in Table 2, our pipeline gen-

eralizes well to different sensor configurations and urban environments. FlexMap achieves 47.0 mAP using the front camera and 48.3 mAP using the rear cameras, outperforming MapTRv2 (Liao et al., 2024) and MapQR (Liu et al., 2024) in both settings.

To evaluate scene-level consistency, we first merge per-view predictions using ground-truth location and camera pose information, and then compute rasterization-based metrics. Our method evaluated on nuScenes validation set achieves 47.30% mIoU on a single front-camera input, compared to 38.10% for GeMap, demonstrating that FlexMap produces geometrically consistent predictions over large scenes.

4.4. Qualitative Analysis

All visualized results of baselines shown here utilize the ground truth camera pose. Figure 5 visualizes predictions across four challenging scenarios. In the urban intersection (row 1), FlexMap correctly detects all pedestrian crossings and accurately predicts lane boundaries and road boundaries matching ground truth geometry. MapQR and MapTRv2 (Liao et al., 2024) mispredict some pedestrian crossings, GeMap (Zhang et al., 2024) hallucinates spurious detections, and MapTR (Liao et al., 2023) produces fragmented pedestrian crossings. On the straight highway (row 2), FlexMap produces clean predictions with consistent lane spacing. The curved road scenario (row 3) tests temporal

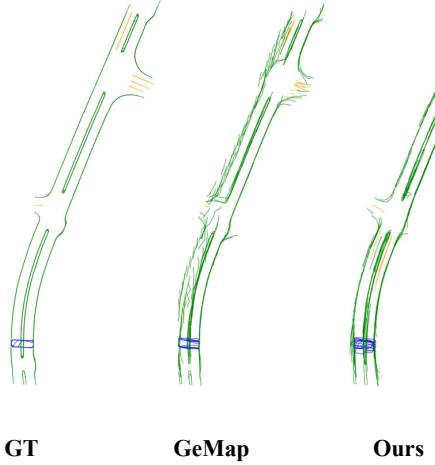


Figure 6. Scene reconstruction quality between (Zhang et al., 2024) and our method. Our approach produces a more coherent global topology with clearer semantic lines.

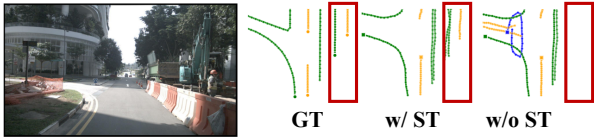


Figure 7. **Ablation of spatial-temporal attention module on nuScenes.** Qualitative comparison showing predictions with spatial-temporal enhancement versus without against ground truth. The module improves temporal and spatial coherence, for example, enabling the model to predict lanes behind occlusions.

consistency and geometric understanding. FlexMap successfully captures smooth road curvature throughout the visible range, with minor localization drift only at the far end, where visual information becomes sparse. Our spatial-temporal attention aggregates motion cues across frames to infer road continuation beyond immediate observations. Baselines show more pronounced fragmentation, with StreamMapNet (Yuan et al., 2024) producing discontinuous lanes. Under heavy tree occlusion (row 4), FlexMap maintains reasonable predictions by leveraging temporal context from preceding frames. MapTRv2 (Liao et al., 2024) shows empty output in cases 3 and 4, because all predicted instances are lower than the confidence threshold.

Figure 6 compares complete scene reconstruction between our method and GeMap (Zhang et al., 2024). FlexMap produces a more coherent vector map with better geometric consistency. Parallel lanes maintain proper separation, intersections exhibit correct connectivity, and the spatial layout aligns more closely with ground truth.

Table 3. Ablation study on nuScenes (Caesar et al., 2020) validation set. A: spatial-temporal attention enhancement; B: camera-aware decoder. All metrics are averaged across configurations.

Variant	A	B	AP _{ped}	AP _{div}	AP _{bou}	mAP
Baseline			30.8	46.9	48.8	42.2
+ A	✓		31.0	50.6	50.3	44.0
+ B		✓	34.2	50.8	52.0	45.7
A + B	✓	✓	36.3	51.7	52.7	46.9

4.5. Ablation Study

Table 3 analyzes the contribution of our two key architectural innovations: (A) spatial-temporal attention enhancement and (B) camera-aware decoder with learned camera tokens. Results are averaged across all configurations on the nuScenes (Caesar et al., 2020) validation set. The baseline model without either component achieves 42.2 mAP. Adding spatial-temporal attention alone improves performance to 44.0 mAP (+1.8), demonstrating that explicit separation of cross-view spatial reasoning and cross-time temporal modeling enhances geometry-aware features. Incorporating the camera-aware decoder alone yields 45.7 mAP (+3.5), indicating that view-adaptive attention mechanisms and camera-conditioned query initialization significantly improve localization accuracy. The full model combining both components achieves 46.9 mAP (+4.7), demonstrating complementary benefits where spatial-temporal attention provides richer contextual features that the camera-aware decoder effectively exploits for map element prediction. Figure 7 provides qualitative evidence, showing that without spatial-temporal enhancement, predictions exhibit temporal inconsistency and poor cross-view alignment, while the full model maintains stable, geometrically coherent predictions across frames.

5. Conclusion

This paper has presented FlexMap, a camera configuration-agnostic framework for vectorized HD map construction, addressing a critical bottleneck for flexible, affordable, and scalable HD mapping deployment across heterogeneous vehicle fleets. By leveraging geometry foundation models and eliminating dependence on explicit camera pose and 2D-to-BEV projection, our approach enables robust map generation across diverse camera setups, from single monocular cameras to flexible multi-camera configurations. The proposed spatial-temporal attention mechanism effectively aggregates cross-view spatial context and temporal dynamics, while the camera-aware decoder with learned camera tokens adapts to view-specific geometric patterns without requiring projection matrices. Experiments demonstrate that FlexMap outperforms existing baselines while maintaining robustness to missing views and sensor variations.

Impact Statement

This paper presents work whose goal is to advance fundamental research in autonomous driving. There are many potential societal consequences of our work, none of which we feel must be specifically highlighted here.

References

ACEA Auto. Average age of the EU vehicle fleet, by country, 2024. URL <https://www.acea.auto/figure/average-age-of-eu-vehicle-fleet-by-country/>.

Applied Intuition. How hybrid mapping enhances ADAS | Applied Intuition, 2025. URL <https://www.appliedintuition.com/blog/hybrid-mapping-strategies>.

Caesar, H., Bankiti, V., Lang, A. H., Vora, S., Lioung, V. E., Xu, Q., Krishnan, A., Pan, Y., Baldan, G., and Bejbom, O. nuScenes: A multimodal dataset for autonomous driving. In *IEEE Conf. Comput. Vis. Pattern Recog.*, 2020.

Chang, M.-F., Lambert, J., Sangkloy, P., Singh, J., Bak, S., Hartnett, A., Wang, D., Carr, P., Lucey, S., Ramanan, D., and Hays, J. Argoverse: 3D Tracking and Forecasting with Rich Maps. In *IEEE Conf. Comput. Vis. Pattern Recog.*, 2019.

Chen, S., Cheng, T., Wang, X., Meng, W., Zhang, Q., and Liu, W. Efficient and Robust 2D-to-BEV Representation Learning via Geometry-guided Kernel Transformer. *arXiv preprint arXiv:2206.04584*, 2022.

Ding, W., Qiao, L., Qiu, X., and Zhang, C. PivotNet: Vectorized Pivot Learning for End-to-end HD Map Construction. In *Int. Conf. Comput. Vis.*, 2023.

Dong, Y., Kang, C., Zhang, J., Zhu, Z., Wang, Y., Yang, X., Su, H., Wei, X., and Zhu, J. Benchmarking Robustness of 3D Object Detection to Common Corruptions in Autonomous Driving. In *IEEE Conf. Comput. Vis. Pattern Recog.*, 2023.

Du, Y., Yang, S., Wang, L., Hou, Z., Cai, C., Tan, Z., Chen, M., Huang, S.-S., and Li, Q. RTMap: Real-Time Recursive Mapping with Change Detection and Localization. *arXiv preprint arXiv:2507.00980v2*, 2025.

Ge, C., Chen, J., Xie, E., Wang, Z., Hong, L., Lu, H., Li, Z., and Luo, P. Metabev: Solving sensor failures for bev detection and map segmentation. *arXiv preprint arXiv:2304.09801*, 2023.

Hao, X., Wei, M., Yang, Y., Zhao, H., Zhang, H., Zhou, Y., Wang, Q., Li, W., Kong, L., and Zhang, J. Is Your HD Map Constructor Reliable under Sensor Corruptions? *arXiv preprint arXiv:2406.12214*, 2024.

Hao, X., Kong, L., Yin, R., Wang, P., Zhang, J., Diao, Y., and Zhao, S. SafeMap: Robust HD Map Construction from Incomplete Observations. In *ICML*, 2025a.

Hao, X., Zhao, Y., Ji, Y., Dai, L., Hao, P., Li, D., Cheng, S., and Yin, R. What Really Matters for Robust Multi-Sensor HD Map Construction? In *IEEE/RSJ International Conference on Intelligent Robots and Systems (IROS)*, 2025b.

Hu, A., Murez, Z., Mohan, N., Dudas, S., Hawke, J., Badri-narayanan, V., Cipolla, R., and Kendall, A. FIERY: Future Instance Prediction in Bird’s-Eye View from Surround Monocular Cameras. In *ICCV*, 2021.

Hu, H., Wang, F., Wang, Y., Hu, L., Xu, J., and Zhang, Z. ADMAP: Anti-disturbance Framework for Vectorized HD Map Construction. In *Eur. Conf. Comput. Vis.*, 2024.

Jiang, L., Mao, Y., Xu, L., Lu, T., Ren, K., Jin, Y., Xu, X., Yu, M., Pang, J., Zhao, F., et al. Anysplat: Feed-forward 3d gaussian splatting from unconstrained views. *ACM Transactions on Graphics (TOG)*, 44(6):1–16, 2025.

Jo, K., Kim, C., and Sunwoo, M. Simultaneous localization and map change update for the high definition map-based autonomous driving car. *Sensors*, 2018.

Keetha, N., Müller, N., Schönberger, J., Porzi, L., Zhang, Y., Fischer, T., Knapitsch, A., Zauss, D., Weber, E., Antunes, N., Luiten, J., Lopez-Antequera, M., Bulò, S. R., Richardt, C., Ramanan, D., Scherer, S., and Kortschieder, P. MapAnything: Universal Feed-Forward Metric 3D Reconstruction. In *3DV*, 2026.

Kim, N., Seong, H., Ji, D., and Jang, S. Unveiling the Hidden: Online Vectorized HD Map Construction with Clip-Level Token Interaction and Propagation. In *NeurIPS*, 2024.

Kong, L., Xie, S., Hu, H., Niu, Y., Ooi, W. T., Cottereau, B. R., Ng, L. X., Ma, Y., Zhang, et al. The RoboDrive Challenge: Drive Anytime Anywhere in Any Condition. In *ICRA*, 2024.

Li, Q., Wang, Y., Wang, Y., and Zhao, H. Hdmapnet: An online hd map construction and evaluation framework. In *Proc. IEEE Intl. Conf. Robot. Autom. (ICRA)*, 2022a.

Li, Z., Wang, W., Li, H., Xie, E., Sima, C., Lu, T., Yu, Q., and Dai, J. BEVFormer: Learning Bird’s-Eye-View Representation from Multi-Camera Images via Spatiotemporal Transformers. In *Eur. Conf. Comput. Vis.*, 2022b.

Liao, B., Chen, S., Wang, X., Cheng, T., Zhang, Q., Liu, W., and Huang, C. Maptr: Structured modeling and learning for online vectorized hd map construction. In *ICLR*, 2023.

Liao, B., Chen, S., Zhang, Y., Jiang, B., Zhang, Q., Liu, W., Huang, C., and Wang, X. Maptrv2: An end-to-end framework for online vectorized hd map construction. In *Int. J. Comput. Vis.*, 2024.

Lin, J., Wang, K., Wang, S., Fan, S., Li, G., and Gao, W. VGD: Visual Geometry Gaussian Splatting for Feed-Forward Surround-view Driving Reconstruction. *arXiv preprint arXiv:2510.19578*, 2025.

Liu, Y., Yuan, T., Wang, Y., Wang, Y., and Zhao, H. VectorMapNet: End-to-end vectorized HD map learning. In *ICML*, 2023a.

Liu, Z., Tang, H., Amini, A., Yang, X., Mao, H., Rus, D., and Han, S. BEVFusion: Multi-Task Multi-Sensor Fusion with Unified Bird's-Eye View Representation. In *ICRA*, 2023b.

Liu, Z., Zhang, X., Liu, G., Zhao, J., and Xu, N. Leveraging Enhanced Queries of Point Sets for Vectorized Map Construction. In *Eur. Conf. Comput. Vis.*, 2024.

Oquab, M., Darcey, T., Moutakanni, T., Vo, H., Szafraniec, M., Khalidov, V., Fernandez, P., Haziza, D., Massa, F., et al. DINOv2: Learning Robust Visual Features without Supervision. *arXiv preprint arXiv:2304.07193*, 2024.

Scheel, O., Bergamini, L., Wołczyk, M., Osiński, B., and Ondruska, P. Urban Driver: Learning to Drive from Real-world Demonstrations Using Policy Gradients. In *CoRL*, 2021.

Shan, T. and Englot, B. LeGO-LOAM: Lightweight and Ground-Optimized Lidar Odometry and Mapping on Variable Terrain. In *IEEE/RSJ International Conference on Intelligent Robots and Systems (IROS)*, 2018.

Shan, T., Englot, B., Meyers, D., Wang, W., Ratti, C., and Rus, D. LIO-SAM: Tightly-coupled Lidar Inertial Odometry via Smoothing and Mapping. In *IEEE/RSJ International Conference on Intelligent Robots and Systems (IROS)*, 2020.

S&P Global Mobility. Fuel for Thought: Average age of vehicles in the US hits new record, 2024. URL <https://www.spglobal.com/automotive-insights/en/blogs/2024/5/fuel-for-thought-average-age-vehicles-2024>.

Vazquez, J. L., Liniger, A., Schwarting, W., Rus, D., and Gool, L. V. Deep Interactive Motion Prediction and Planning: Playing Games with Motion Prediction Models. In *L4DC*, 2022.

Wang, J., Chen, M., Karaev, N., Vedaldi, A., Rupprecht, C., and Novotny, D. VGGT: Visual Geometry Grounded Transformer. In *IEEE Conf. Comput. Vis. Pattern Recog.*, 2025.

Wang, S., Jia, F., Liu, Y., Zhao, Y., Chen, Z., Wang, T., Zhang, C., Zhang, X., and Zhao, F. Stream Query Denoising for Vectorized HD Map Construction. In *Eur. Conf. Comput. Vis.*, 2024a.

Wang, S., Leroy, V., Cabon, Y., Chidlovskii, B., and Revaud, J. DUS3R: Geometric 3D Vision Made Easy. In *IEEE Conf. Comput. Vis. Pattern Recog.*, 2024b.

Wijaya, B., Jiang, K., Yang, M., Wen, T., Wang, Y., Tang, X., Fu, Z., Zhou, T., and Yang, D. High definition map mapping and update: A general overview and future directions. *arXiv preprint arXiv:2409.09726*, 2024.

Wilson, B., Qi, W., Agarwal, T., Lambert, J., Singh, J., Khandelwal, S., Pan, B., Kumar, R., Hartnett, A., Pontes, J. K., Ramanan, D., Carr, P., and Hays, J. Argoverse 2: Next Generation Datasets for Self-Driving Perception and Forecasting. In *Proceedings of the Neural Information Processing Systems Track on Datasets and Benchmarks*, 2023.

Wu, K., Yang, C., and Li, Z. Interactionmap: Improving online vectorized hdmap construction with interaction. *arXiv preprint arXiv:2503.21659*, 2025.

Yuan, T., Liu, Y., Wang, Y., Wang, Y., and Zhao, H. Streammapnet: Streaming mapping network for vectorized online hd map construction. In *Proc. WACV*, 2024.

Zhang, L., Hao, X., Xu, Q., Zhang, Q., Zhang, X., Wang, P., Zhang, J., Wang, Z., Zhang, S., and Xu, R. MapNav: A Novel Memory Representation via Annotated Semantic Maps for Vision-and-Language Navigation. *arXiv preprint arXiv:2502.13451*, 2025.

Zhang, Z., Zhang, Y., Ding, X., Jin, F., and Yue, X. Online vectorized hd map construction using geometry. In *Eur. Conf. Comput. Vis.*, 2024.

Zhou, B. and Krähenbühl, P. Cross-view Transformers for real-time Map-view Semantic Segmentation. In *IEEE Conf. Comput. Vis. Pattern Recog.*, 2022.

Zhou, Y., Zhang, H., Yu, J., Yang, Y., Jung, S., Park, S.-I., and Yoo, B. Himap: Hybrid representation learning for end-to-end vectorized hd map construction. In *IEEE Conf. Comput. Vis. Pattern Recog.*, 2024.

Zhu, X., Su, W., Lu, L., Li, B., Wang, X., and Dai, J. Deformable DETR: Deformable Transformers for End-to-End Object Detection. In *ICLR*, 2021.

Zhu, Z., Zhang, Y., Chen, H., Dong, Y., Zhao, S., Ding, W., Zhong, J., and Zheng, S. Understanding the Robustness

of 3D Object Detection with Bird’s-Eye-View Representations in Autonomous Driving. In *IEEE Conf. Comput. Vis. Pattern Recog.*, 2023.

Zuo, S., Xie, Z., Zheng, W., Xu, S., Li, F., Jiang, S., Chen, L., Yang, Z.-X., and Lu, J. Dvgt: Driving visual geometry transformer. *arXiv preprint arXiv:2512.16919*, 2025.

A. Appendix

We first provide additional explanation about data processing and the experimental setup. Then, we show the additional quantitative and qualitative results for different configurations on the nuScenes Dataset (Caesar et al., 2020) and add additional scene-level comparison.

A.1. Additional Details About Experimental Setup

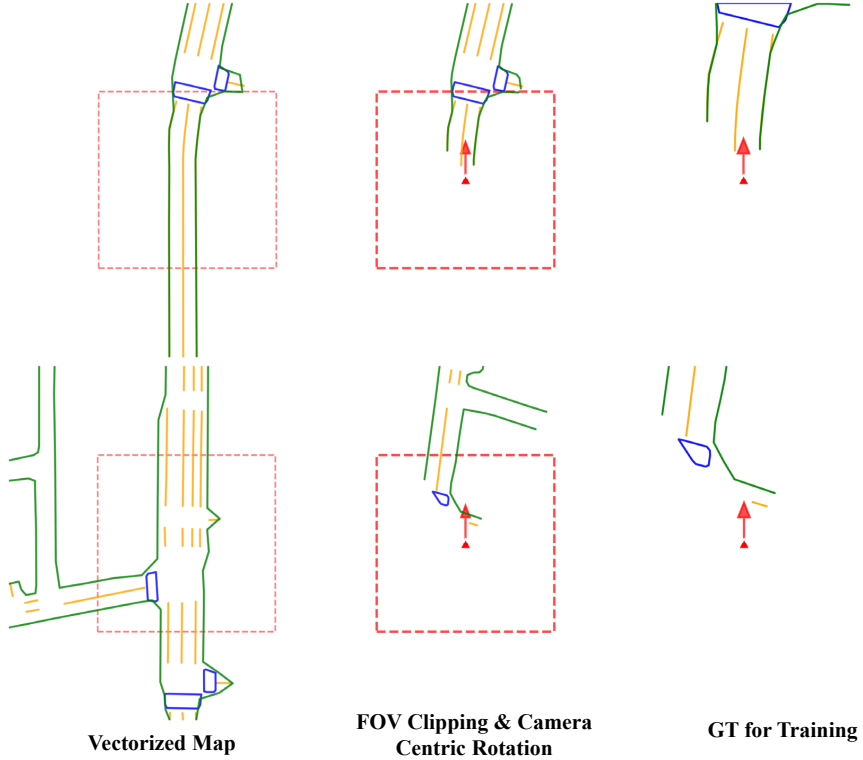


Figure 8. Scene reconstruction quality between baselines and our method using a single front camera as input. Our approach produces a more coherent global topology with clearer semantic lines.

Data Processing. To train our model with camera-centric representations, we employ a robust four-step ground truth processing pipeline that ensures consistent map coverage across all camera views, regardless of camera orientation. The pipeline, illustrated in Figure 8, operates as follows:

Step 1: Large Patch Extraction (120×120m). We first extract a large 120×120m Bird’s Eye View (BEV) map patch centered at the ego vehicle’s LiDAR position. This double-sized patch (compared to our final 60×60m target) ensures sufficient map content survives the subsequent rotation step, particularly for cameras oriented at extreme angles (e.g., rear-facing cameras).

Step 2: Camera FOV Clipping. We apply camera-specific field-of-view (FOV) clipping in 3D camera space. Points are clipped if they fall outside the camera’s horizontal FOV. This removes map elements that would not be visible to the camera.

Step 3: Camera-Centric Rotation. The FOV-clipped vectors are rotated to align with camera-centric coordinates, where the camera’s forward direction corresponds to the +Y axis. This transformation ensures that each camera view’s ground truth is in a consistent coordinate frame, enabling multi-camera training where different cameras have different orientations.

Step 4: Final Cropping (60×60m). After rotation, we re-crop the vectors to the final 60×60m region. This pipeline differs from evaluation-time processing used by prior works (Liao et al., 2023; Zhang et al., 2024), which typically extract maps directly at the target size (30×60m). Our double-patch approach is essential for training with all six camera views simultaneously, as it prevents loss of map content during rotation to camera-centric coordinates.

Evaluation Metrics. For fair comparison with baseline methods, we process their predictions to match our evaluation protocol, as shown in Figure 9. Baseline methods (MapTR (Liao et al., 2023), MapTRv2 (Liao et al., 2024), StreamMapNet (Yuan et al., 2024), GeMap (Zhang et al., 2024)) output predictions in ego-centric BEV coordinates. We transform these predictions to camera-centric coordinates and apply the same FOV clipping used in our ground truth processing. This ensures that all methods are evaluated on the same visible map region for each camera view. Predictions are then matched against ground truth using the same matching cost and thresholds (Chamfer distance $\tau \in \{0.5, 1.0, 1.5\}$ m) following MapTR’s evaluation protocol (Liao et al., 2023).

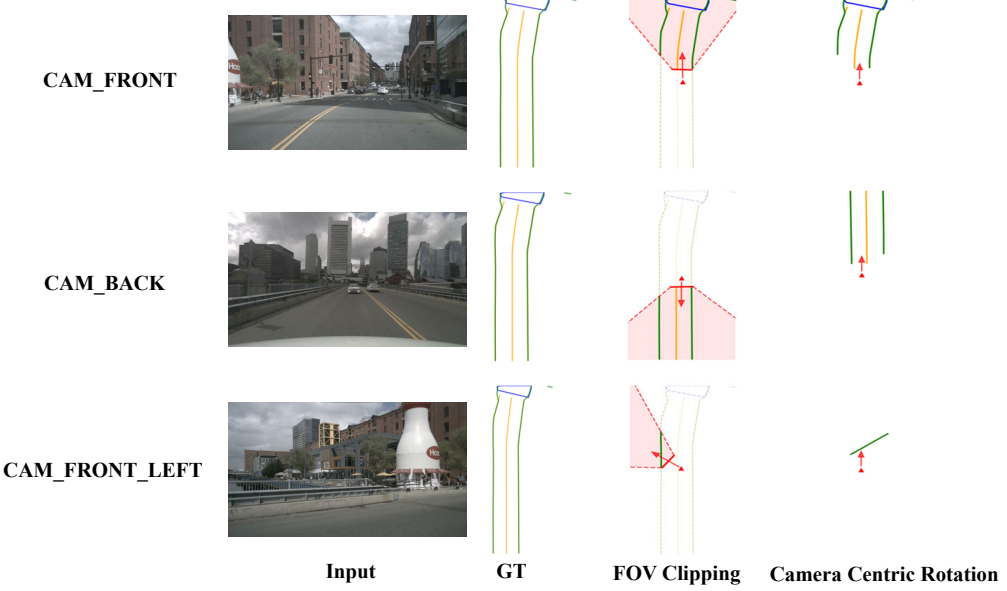


Figure 9. Scene reconstruction quality between baselines and our method using a single front camera as input. Our approach produces a more coherent global topology with clearer semantic lines.

A.2. Additional Quantitative Results

Table 4 provides additional results on the nuScenes (Caesar et al., 2020) validation set under multiple input-camera settings. Unless stated otherwise, all metrics are computed per view after applying camera-centric rotation and FOV clipping. For baselines that require camera pose, we supply ground-truth camera pose in this table to isolate the upper-bound performance of pose-conditioned systems.

Table 4. nuScenes (Caesar et al., 2020) validation results with ground-truth camera poses for baselines. Baselines use ground-truth poses; our method remains pose-free. Results are reported for different camera input settings. For **Front/Back 3 PVs**, the input consists of three front-facing views $\{F, FL, FR\}$ or three back-facing views $\{B, BL, BR\}$. All methods are evaluated per view after camera-centric alignment and FOV clipping (Section A.1).

Method	Front only (1PV)				Back only (1PV)				Front+Back (2PV)				Front/Back 3 PVs			
	AP _{ped}	AP _{div}	AP _{bou}	mAP	AP _{ped}	AP _{div}	AP _{bou}	mAP	AP _{ped}	AP _{div}	AP _{bou}	mAP	AP _{ped}	AP _{div}	AP _{bou}	mAP
MapTR (Liao et al., 2023)	22.7	49.8	47.8	40.1	23.4	49.1	47.4	39.9	25.1	55.3	55.7	45.4	29.2	45.4	46.8	40.5
MapTRv2 (Liao et al., 2024)	16.7	44.3	43.3	34.8	29.3	41.5	45.6	38.8	22.7	53.6	55.0	43.8	33.5	44.7	48.3	42.2
SMN (Yuan et al., 2024)	9.5	36.5	34.1	26.7	20.3	47.1	32.4	33.3	18.5	55.9	51.1	41.8	25.6	51.5	45.8	41.0
GeMap (Zhang et al., 2024)	24.0	50.9	48.9	41.2	23.4	46.2	48.8	39.5	27.1	59.3	58.4	48.3	27.8	53.9	52.9	44.9
MapQR (Liu et al., 2024)	16.8	42.0	38.1	32.3	21.8	54.5	45.8	40.7	24.0	63.2	61.2	49.5	34.3	56.9	55.1	48.8
Ours	42.1	53.6	51.9	49.2	31.4	50.1	52.3	44.6	36.4	52.6	51.7	46.9	35.1	50.6	54.8	46.8

A.3. Additional Qualitative Results

Figure 10 visualizes scene-level reconstructions on nuScenes (Caesar et al., 2020) using a single front camera as input. The qualitative comparisons are rendered after applying the same camera-centric alignment and FOV clipping used in

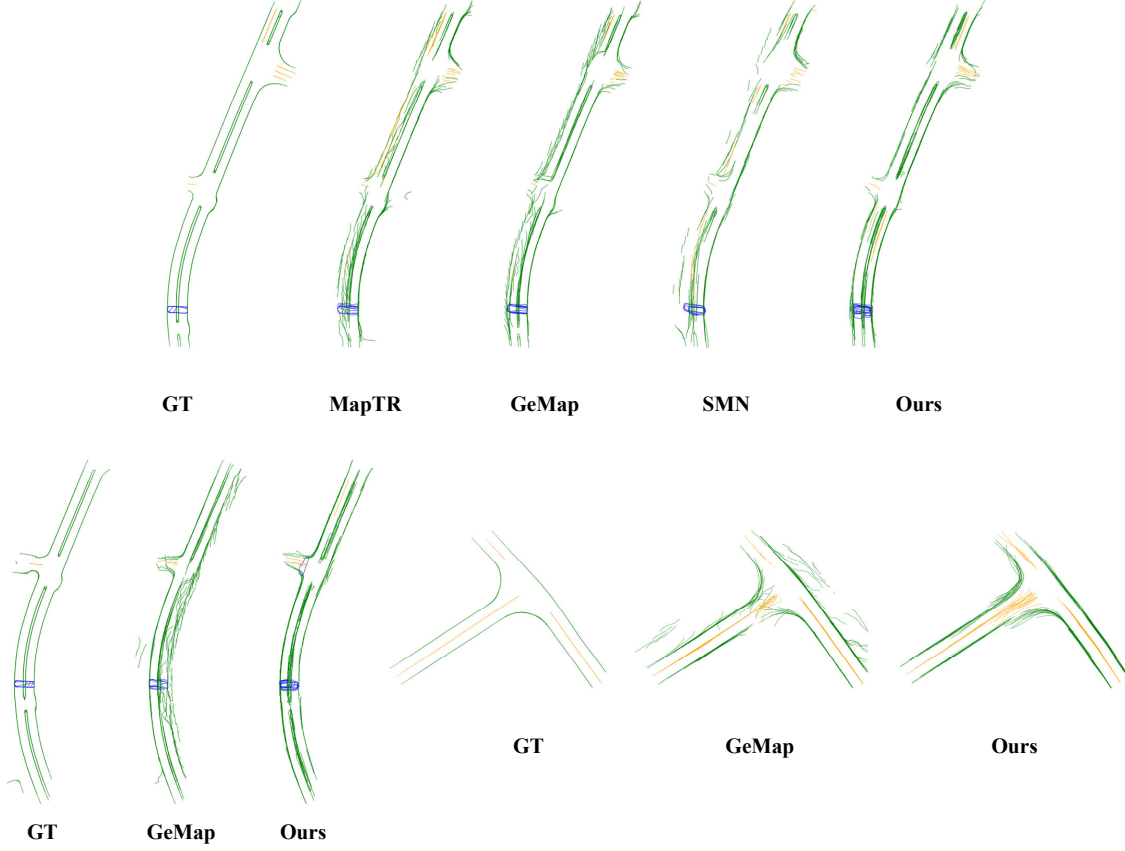


Figure 10. Qualitative comparison on nuScenes (Caesar et al., 2020) with front-only input. We visualize scene-level reconstructions from baselines and our method using a single front camera. Baselines are rendered using ground-truth poses for alignment, while our method does not take camera pose as input. Overall, our predictions exhibit cleaner topology, fewer fragmented dividers, and more consistent boundary connectivity.

our evaluation protocol, so the shown map elements correspond to the visible region of the camera view. Overall, our method produces cleaner long-range topology and fewer fragmented map segments near the FOV boundary, yielding clearer semantic structure in lane dividers, boundaries, and pedestrian crossings.